



Contents lists available at ScienceDirect

Journal of Sound and Vibration

journal homepage: www.elsevier.com/locate/jsv



Vibration properties and optimized design of a nonlinear acoustic metamaterial beam

Peng Sheng, Xin Fang, Jihong Wen*, Dianlong Yu

Laboratory of Science and Technology on Integrated Logistics Support, College of Intelligence Science and Technology, National University of Defense Technology, Changsha, Hunan 410073, China



ARTICLE INFO

Article history:

Received 4 August 2020

Accepted 21 September 2020

Available online 13 October 2020

Keywords:

Nonlinear acoustic metamaterials

Vibration reduction

Optimized design

ABSTRACT

Lightweight, low-frequency, broadband and highly efficient vibration reduction is widely desired in various devices. Nonlinear acoustic metamaterial (NAM) is a new type of metamaterial that may possess these vibration reduction features. However, the laws governing the manipulation of the NAM vibration response and its optimized design have not been addressed. This paper numerically and experimentally studies the manipulation laws and optimized design of the NAM beam reported in [Nature Comm., 8: 1288(2017)]. The strongly nonlinear metacell consists of three bridging-coupled resonators: A Duffing oscillator, a flexural resonator and a vibro-impact resonator. Both time-domain and frequency-domain finite element models are established to calculate the vibrations of the beam. We systematically study the influences of the amplitude, nonlinear stiffness coefficients, resonance frequencies, mass and beam thickness on the bandwidth and efficiency of its vibration reduction properties. Moreover, based on these laws, we present an optimized lightweight NAM beam to realize the low-frequency, broadband and highly efficient vibration reduction with the greatly reduced attached mass. Finally, different NAM samples are fabricated to verify the efficient reduction effect. This work could support the study, creation and application of NAMs in the future.

© 2020 Elsevier Ltd. All rights reserved.

1. Introduction

Lightweight, low-frequency, broadband and highly efficient vibration reduction is a widely desired technology for various devices. Acoustic metamaterials (AMs) are typically artificial periodic media structured on a size scale smaller than the wavelength of external stimuli [1–4]. At present, numerous studies have focused on linear AMs [5–9]. Nonlinear acoustic metamaterials (NAMs) are metamaterials with nonlinear dynamic effects. In recent years, the properties of NAMs have become increasingly studied.

For discrete nonlinear models, the band edge mode [10] and equivalent negative mass density characteristics [11] of nonlinear diatomic chain model [12] were studied. By analyzing spatial wave packet propagation [13,14] in an infinitely large and weakly nonlinear structure, it was found that the transient wave packet exhibits a significant frequency shift when propagating within the band gap. A linear locally resonant unit cell was implanted into a hollow spherical shell to form NAMs [15], and its band gap and vibration reduction characteristics were studied, and then the harmonics in the band gap was found. The 1/2 harmonic attenuation region near the fundamental frequency exhibits in NAMs, and the formation

* Corresponding author.

E-mail address: wenjihong@vip.sina.com (J. Wen).

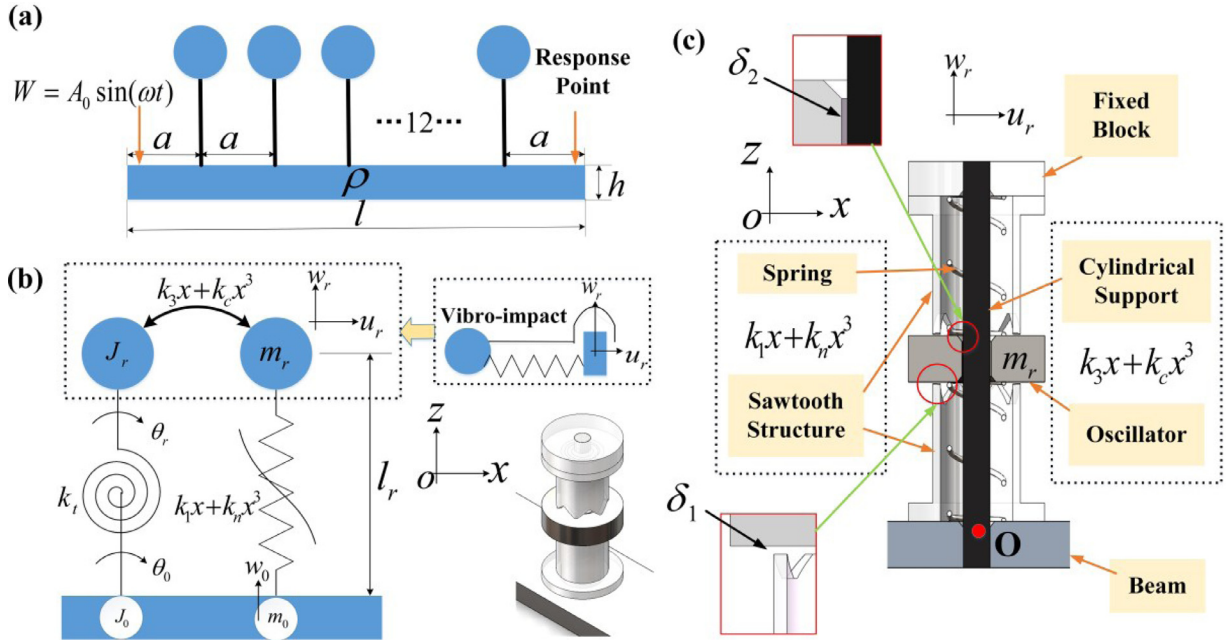


Fig. 1. NAM beam model. (a) Theoretic NAM beam model; (b) theoretic locally resonant unit cell; (c) diagrammatic sketch of the locally resonant unit cell.

mechanism of the subharmonic attenuation band was revealed by a semi-analytical analysis based on the perturbation method [16].

For the continuum nonlinear model, the approximate dispersion characteristics [17,18] of one-dimensional (1D) nonlinear locally resonant metamaterial can be obtained based on the transfer matrix method [19], and the results showed that the position and width of the band gap vary with the amplitude. Coupling an oscillator with the magnetic force can produce the geometric nonlinearity [20], which can realize a transistor-like phonon switch element [21,22]. Fang et al. [23] constructed a nonlinear locally resonant unit cell coupled by torsion resonance, magnetic nonlinear resonance and gap collision strong nonlinear resonance and designed a 1D NAM beam structure and a 2D NAM plate structure. On this basis, the study found that strongly NAMs have self-growing band gaps and an adaptive-broadening band [24], which breaks through the understanding of traditional linear and nonlinear band structures [25,26]. In order to analyze the transient dynamics [27] of nonlinear locally resonant metamaterials, the homogenization method of transient computation [28] is extended to nonlinear dynamics.

Studies have shown that under strongly nonlinear conditions, due to the bifurcation [29] of periodic solutions, the periodic vibration responses in the passbands of NAMs become chaotic responses. According to the bridging-coupling principle of a nonlinear locally resonant (NLR) band gap [30], increasing the frequency distance between two NLR band gaps can improve the elastic wave reduction efficiency and total attenuation bandwidth in the chaotic bands [31,32]. By using the principle of bridging-coupling, the chaotic bands of NAMs can be regulated, and the bandwidth limitation of the vibration reduction of linear metamaterials can be overcome.

However, there are some problems plaguing the application of NAMs, especially the large attached mass, difficulty in structural design, and lack of experimental cases. Solutions of these problems rely on the manipulation laws of the vibration responses and optimized design for efficient vibration reduction. This paper establishes a NAM beam model, analyzes the manipulation laws of parameters and then optimizes the design to achieve lightweight, low-frequency, broadband, and highly efficient vibration reduction. Experiments are carried out to demonstrate these analyses.

2. NAM beam model

The one-dimensional NAM beam considered in this work is shown in Fig. 1(a). It consists of a primary beam and periodic resonators, where the thickness of the beam is h , the beam length is l , the beam width is b , the material density is ρ , the Young's modulus of material is E_0 , the Poisson's ratio of material is μ , and the lattice constant is a . The deformation of the primary beam is linear, and nonlinearity arises from the attached resonators. In our paper, the length of the NAM beam is limited to 12 cells.

Fang et al. [23] designed NAMs with a strongly nonlinear metacell consisting of a Duffing oscillator, a flexural resonator and a vibro-impact resonator. This paper adopts a similar theoretical design scheme, as shown in Fig. 1(b), but the physical realization of these nonlinear resonators (see Fig. 1(c)) are essentially different from that reported in [23]. We adopt the

lumped parameter system to establish the theoretical model of the nonlinear resonators. In this work, the resonant unit cell consists of a cylindrical strut, a steel oscillator, two springs, two sawtooth rubber structures, and a top block. The strut is used to support the whole structure. Its top end is connected to the fixed block and the other end is connected to the primary beam through glue. The mass of the steel oscillator is m_r . We connect the oscillator to the fixed block and the beam with two identical springs, whose constant stiffness is k_1 . The sawtooth structure is a thin-wall cylinder and its sawtooth is set near the oscillator. The spring is put into the sawtooth cylinder. A clearance δ_1 is left between the sawtooth structure and the oscillator. When the oscillator m_r contacts the sawtooth, its stiffness in the transverse direction increases harshly: nonlinearity appears. We adopt a smooth cubic function $k_1x+k_nx^3$ to approximate the nonlinear force in this process, i.e., Duffing oscillator, where k_n is the nonlinear stiffness coefficient. The rubber sawtooth is used to make the real force be “smoother”.

As described above, the motion equations of the resonators in transverse direction are

$$\begin{cases} m_r \ddot{w}_r = -k_1(w_r - w_0) - k_n(w_r - w_0)^3 - c(\dot{w}_r - \dot{w}_0) \\ (m_0 + \rho a)\ddot{w}_0 = k_1(w_r - w_0) + k_n(w_r - w_0)^3 + c(\dot{w}_r - \dot{w}_0) + F(t) \end{cases} \quad (1)$$

where w_r and w_0 are the transverse displacements of masses m_r and m_0 , respectively; c is the damping coefficient; $F(t)$ is the coupling force between the primary beam and the resonators. $F(t)$ is generated by the shear stress of the beam. Let $z_r = w_r - w_0$, one obtains

$$\begin{cases} m_r(\ddot{z}_r + \ddot{w}_0) = -k_1 z_r - k_n z_r^3 - c \dot{z}_r \\ (m_0 + \rho a)\ddot{w}_0 + m_r(\ddot{z}_r + \ddot{w}_0) = F(t) \end{cases} \quad (2)$$

Moreover, the strut can generate flexural vibration that drives the block and the oscillator rotate around point O. In this motion, the strut acts as a torsion spring, k_t , and the block and rod generate the moment of inertia J_0 and J_r . J_0 and J_r can be derived with finite element simulations. Importantly, a clearance δ_2 is left between the oscillator and the strut. Therefore, the oscillator m_r collides with the strut when m_r vibrates along the horizontal direction as labeled by u_r in Fig. 1(b). Thus, vibro-impact nonlinearity arises in this process. We still use Duffing equation, $k_3x+k_cx^3$, to approximate this nonlinear force applied on m_r , where k_3 and k_c are the linear and nonlinear stiffness coefficients, respectively. In the mathematical model in Fig. 1(b), m_0 and J_0 denotes the attached mass and moment of inertia at point O, respectively. The nonlinear motion equations for the coupled torsional system are

$$\begin{cases} J_0 \ddot{\theta}_0 = k_t(\theta_r - \theta_0) + M_0(t) \\ J_r \ddot{\theta}_r + m_r l_r \ddot{u}_r = -k_t(\theta_r - \theta_0) \\ m_r \ddot{u}_r = -k_3(u_r - l_r \theta_r) - k_c(u_r - l_r \theta_r)^3 \end{cases} \quad (3)$$

where θ_r and θ_0 are the torsional angles J_r and J_0 , respectively; u_r is the x -axes displacement of mass m_r ; $M_0(t)$ is the coupling torque between the beam and the attached inertia J_0 ; l_r is the lateral distance between m_r and the beam. Let $x_r = u_r - l_r \theta_r$, we obtain

$$\begin{cases} J_0 \ddot{\theta}_0 = k_t(\theta_r - \theta_0) + M_0(t) \\ J_r \ddot{\theta}_r + m_r l_r (\ddot{x}_r + l_r \ddot{\theta}_r) = -k_t(\theta_r - \theta_0) \\ m_r (\ddot{x}_r + l_r \ddot{\theta}_r) = -k_3 x_r - k_c x_r^3 \end{cases} \quad (4)$$

In simulation and experiment, a transversal sinusoidal wave $W = A_0 \sin \omega t$ is applied on the left end of the primary beam, and other part is free, where ω denotes the driving angular frequency, f denotes the driving frequency. The responses of the right end are measured. The vibration transmission H is defined as

$$H = 20 \log_{10}(W_b/A_0) \text{dB} \quad (5)$$

where A_0 is the vibration amplitude of the excitation point, which is used as a reference value. W_b is the vibration amplitude of the response point.

The initial values of the parameters (before optimization) are listed in Table 1.

The dispersion curve of linear metamaterial beam is shown in Fig. 2. It can be seen that the linear beam has two locally resonant bandgaps in the range of 0–500 Hz: LR1 and LR2. LR1 derives from the linearized Duffing resonator, and LR2 derives from the torsional resonator. In addition, there is a Bragg bandgap in the range of 800–1500 Hz. There is a line at 12.65 Hz, which is a low-frequency resonance, but it has almost no effect on the vibration characteristics.

3. Finite element methods

Based on the motion equations of the resonators and beam element (the finite element matrices are shown in Appendix B), we establish the finite element model (FEM) of the NAM beam consisting of 12 locally resonant unit cells. The motion differential equation of the whole structure can be obtained as

$$\mathbf{M}\ddot{\mathbf{x}} + \mathbf{C}\dot{\mathbf{x}} + \mathbf{K}\mathbf{x} + \mathbf{N}\mathbf{x}^3 = \mathbf{F} \quad (6)$$

Table 1
Model parameters.

Symbol	Definition	Value	Symbol	Definition	Value
a	Lattice constant	80 mm	J_r	Moment of inertia	2.225e-5 kg m ²
m_0	Lumped mass	15 g	l	Beam length	1040 mm
m_r	Oscillator mass	10 g	b	Beam width	20 mm
k_1	Linear coefficient	631.65 N m ⁻¹	h	Beam thickness	4 mm
k_n	Nonlinear coefficient	3.276e6 N m ⁻³	ρ	Beam density	2780 kg m ⁻³
k_t	Torsional coefficient	44.874 N m rad ⁻¹	E_0	Young's modulus	70 GPa
k_c	Torsional nonlinear coefficient	1e10 N m ⁻³	μ	Poisson's ratio	0.3
k_3	Linear coefficient	63.165 N m ⁻¹	l_r	Oscillator height	20.5 mm
J_0	Lumped moment of inertia	5.75e-7 kg m ²	c	Damping coefficient	0.001
A_0	Excitation amplitude	0.2 mm			

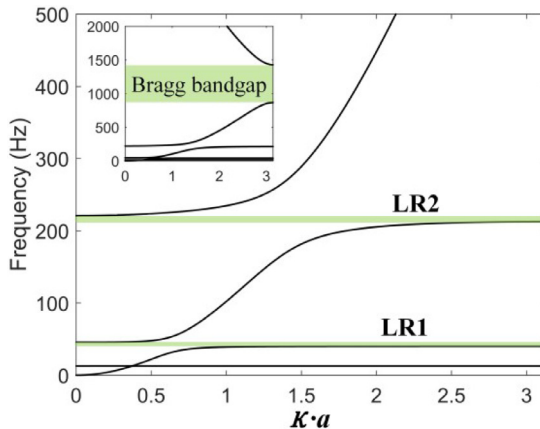


Fig. 2. The dispersion curve of linear metamaterial beam. Where κ denotes the wave vector, a is the lattice constant. The three shaded area represent the band gap range.

in which the displacement vector is

$$\mathbf{x} = \{w_1, \theta_1, \dots, w_{27}, \theta_{27}, w_{r1}, \theta_{r1}, u_{r1}, \dots, w_{r12}, \theta_{r12}, u_{r12}\} \quad (7)$$

And there are 90 degrees of freedom in this vector. \mathbf{M} , \mathbf{C} , \mathbf{K} , \mathbf{N} and \mathbf{F} denote the mass matrix, damping matrix, stiffness matrix, nonlinear stiffness matrix and driving vector, respectively.

In the simulation, the prescribed input displacement $x_1=A_0\sin(\omega t)$ is applied on the left end of the NAM beam. We use the block matrices to transform the equation.

$$\mathbf{M} = \begin{bmatrix} \mathbf{M}_{11} & \mathbf{M}_{1n} \\ \mathbf{M}_{n1} & \mathbf{M}_{nn} \end{bmatrix}, \mathbf{C} = \begin{bmatrix} \mathbf{C}_{11} & \mathbf{C}_{1n} \\ \mathbf{C}_{n1} & \mathbf{C}_{nn} \end{bmatrix}, \mathbf{K} = \begin{bmatrix} \mathbf{K}_{11} & \mathbf{K}_{1n} \\ \mathbf{K}_{n1} & \mathbf{K}_{nn} \end{bmatrix}, \mathbf{N} = \begin{bmatrix} \mathbf{N}_{11} & \mathbf{N}_{1n} \\ \mathbf{N}_{n1} & \mathbf{N}_{nn} \end{bmatrix}, \mathbf{F} = \begin{bmatrix} \mathbf{F}_1 \\ \mathbf{F}_n \end{bmatrix}, \mathbf{x} = \begin{bmatrix} x_1 \\ \mathbf{x}_n \end{bmatrix} \quad (8)$$

Therefore, Eq. (6) can be rewritten as

$$\begin{cases} \mathbf{M}_{11}\ddot{x}_1 + \mathbf{M}_{1n}\ddot{\mathbf{x}}_n + \mathbf{C}_{11}\dot{x}_1 + \mathbf{C}_{1n}\dot{\mathbf{x}}_n + \mathbf{K}_{11}x_1 + \mathbf{K}_{1n}\mathbf{x}_n + \mathbf{N}_{11}x_1^3 + \mathbf{N}_{1n}\mathbf{x}_n^3 = \mathbf{F}_1 \\ \mathbf{M}_{n1}\ddot{x}_1 + \mathbf{M}_{nn}\ddot{\mathbf{x}}_n + \mathbf{C}_{n1}\dot{x}_1 + \mathbf{C}_{nn}\dot{\mathbf{x}}_n + \mathbf{K}_{n1}x_1 + \mathbf{K}_{nn}\mathbf{x}_n + \mathbf{N}_{n1}x_1^3 + \mathbf{N}_{nn}\mathbf{x}_n^3 = \mathbf{F}_n = \mathbf{0} \end{cases} \quad (9)$$

in which only the second equation is needed to solve the response of the metamaterial beam.

$$\mathbf{M}_{nn}\ddot{\mathbf{x}}_n + \mathbf{C}_{nn}\dot{\mathbf{x}}_n + \mathbf{K}_{nn}\mathbf{x}_n + \mathbf{N}_{nn}\mathbf{x}_n^3 = -\mathbf{M}_{n1}\ddot{x}_1 - \mathbf{C}_{n1}\dot{x}_1 - \mathbf{K}_{n1}x_1 - \mathbf{N}_{n1}x_1^3 \quad (10)$$

where $x_1=A_0\sin(\omega t)$, $\dot{x}_1=\omega A_0\cos(\omega t)$, $\ddot{x}_1=-\omega^2 A_0\sin(\omega t)$.

For strongly nonlinear systems, the Eq. (10) can be solved in two ways: numerical integration in time domain and approximate solution in frequency domain. The frequency-domain FEM (FD-FEM) solution can be derived with the harmonic balance method [33]. In this case, let the solution of the system be

$$\mathbf{x}_n = \mathbf{a} \cos(\omega t) + \mathbf{b} \sin(\omega t) \quad (11)$$

A system of algebraic equations can be obtained by applying first-order harmonic balance:

$$\begin{cases} [\mathbf{K}_{nn} - \omega^2 \mathbf{M}_{nn}] \mathbf{a} + \omega \mathbf{C}_{nn} \mathbf{b} + 3 \mathbf{N}_{nn} ((\mathbf{a}^2 + \mathbf{b}^2) \mathbf{a}) / 4 = -\omega A_0 \mathbf{C}_{n1} \\ [\mathbf{K}_{nn} - \omega^2 \mathbf{M}_{nn}] \mathbf{b} - \omega \mathbf{C}_{nn} \mathbf{a} + 3 \mathbf{N}_{nn} ((\mathbf{a}^2 + \mathbf{b}^2) \mathbf{b}) / 4 = -(\mathbf{K}_{n1} - \omega^2 \mathbf{M}_{n1}) A_0 - 3 A_0^3 \mathbf{N}_{n1} / 4 \end{cases} \quad (12)$$

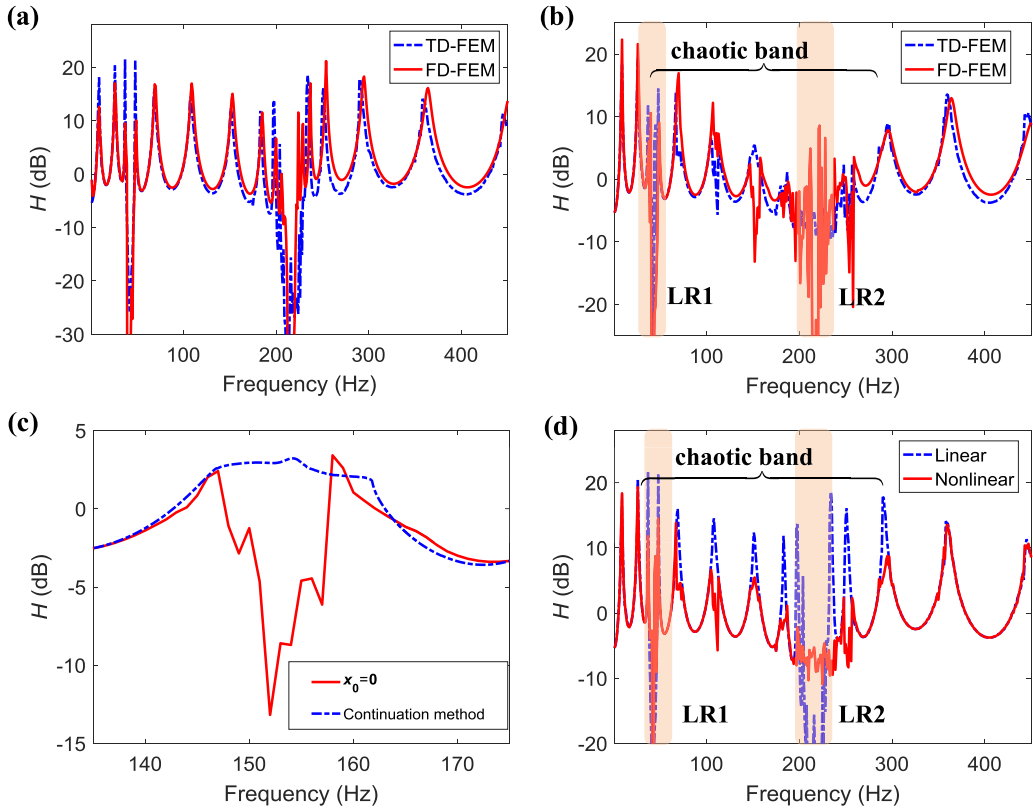


Fig. 3. Finite element simulation results. (a) Comparison of the vibration transmissions obtained by the TD-FEM and FD-FEM: the linear model; (b) comparison of the vibration transmissions obtained by the TD-FEM and FD-FEM: the nonlinear model; (c) comparison of initial value $x_0=0$ in Newton iteration and continuation method; (d) comparison of the time-domain responses of the linear and nonlinear metamaterial beams.

Furthermore, Newton iteration algorithm is used to solve the algebraic equations by specifying an initial value \mathbf{x}_0 of the vector \mathbf{x}_n . There are two ways for \mathbf{x}_0 . One is specifying $\mathbf{x}_0=\mathbf{0}$. In this case, convergent solution can be obtained in most frequency ranges. The other way is adopting the continuation method to obtain converge solution. However, it difficult to use the continuation method in the whole frequency range.

This paper also adopts the time-domain nonlinear FEM (TD-FEM) based on COMSOL to calculate the time-domain responses, as described in Appendix A. Strictly speaking, numerical integration in time domain provides the exact solution of a nonlinear system, which presents the entire evolution process of waves. To prove the accuracy of the harmonic balance method, this paper compares TD-FEM and FD-FEM solutions of both linear and nonlinear acoustic metamaterial beam. The vibration transmissions of the linear model are shown in Fig. 3(a), and the results of TD-FEM and FD-FEM are approximately equal. The small disagreement of low-frequency peaks mainly arising from the simulation time in TD-FEM method: As the low-frequency period is long, it requires longer time to converge to the steady responses but the simulation time is finite in practice. This small inconsistent value has little influence on the response higher than 50 Hz.

The vibration transmissions of the nonlinear model are shown in Fig. 3(b). Here the FD-FEM is solved with the harmonic balance method by specifying $\mathbf{x}_0=\mathbf{0}$. The tendency of the results obtained by TD-FEM and FD-FEM is almost the same, and the second bandgap values obtained by TD-FEM is larger than obtained by FD-FEM. The difference near resonant peak is due to the fact that the FD-FEM solution does not converge for $\mathbf{x}_0=\mathbf{0}$. As shown in Fig. 3(c), using the continuation method instead of $\mathbf{x}_0=\mathbf{0}$ in Newton iteration can present convergent result to make the curve smooth. Fortunately, some non-convergence points for $\mathbf{x}_0=\mathbf{0}$ do not affect the whole law and mechanism, so we adopt this approach in the following research.

The linear and nonlinear results obtained by time-domain simulation are shown in Fig. 3(d). The locally resonant bandgaps $LR1=38\text{--}45$ Hz, $LR2=200\text{--}230$ Hz. There are dense resonances in the passband of the linear metamaterial. For the NAM beam, $LR1$ is slightly narrow; there is still a “bandgap” at $LR2$, but the responses in this range are much higher than those of the linear model because of the nonlinear effects. An interesting feature lies in the passbands: the resonant peaks of the nonlinear model are greatly reduced relative to those of the linear model (as shown in Fig. 3(d)). This effect refers to the chaotic band [29,31]: the chaotic responses of nonlinear vibrations. In NAMs, chaotic bands are those passbands in which an incident low-frequency periodic wave becomes a chaotic emerging wave, reducing wave transmission [29]. The chaotic band has been demonstrated to realize ultralow and ultrabroadband wave reduction in the passbands of NAM. This

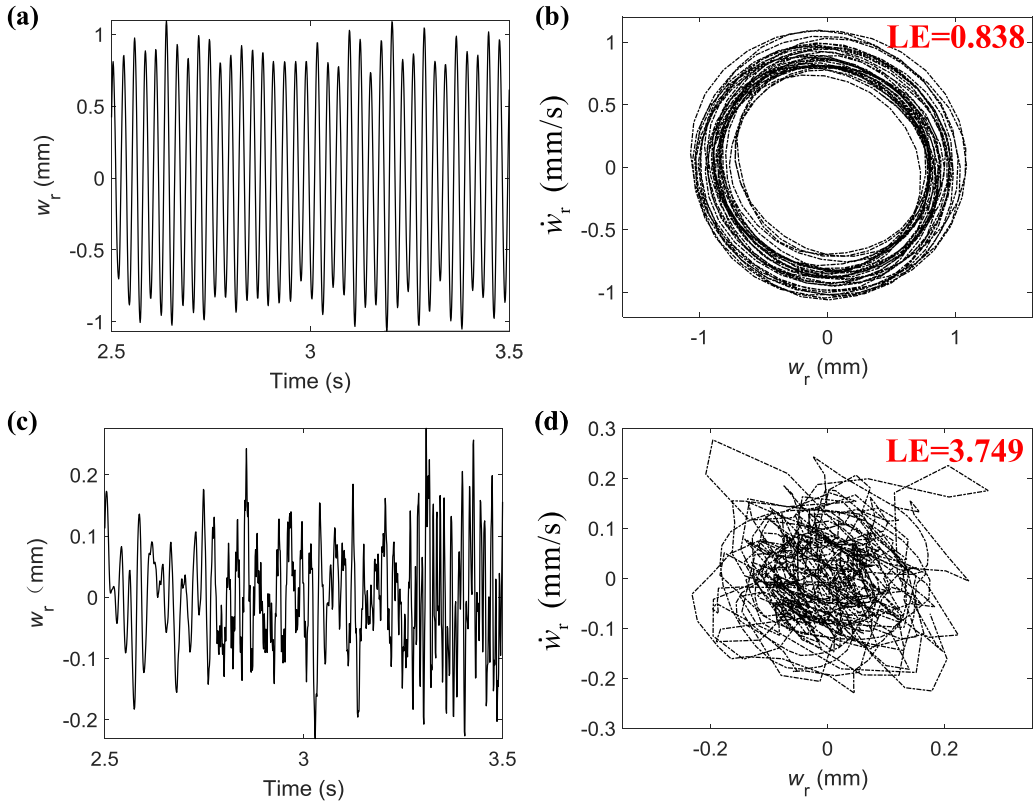


Fig. 4. Time-domain responses and phase diagrams under single-frequency sinusoidal excitation. (a) Time-domain response of the resonant: $f = 37.06$ Hz; (b) the phase diagram and maximal Lyapunov exponent (LE); $f = 37.06$ Hz; (c) time-domain response of the band gap; $f = 44.56$ Hz; (d) the phase diagrams and maximal Lyapunov exponent: $f = 44.56$ Hz.

paper mainly focuses on the responses in the chaotic band. We adopt the Lyapunov exponent (LE) [34] to characterize the chaotic response, where a positive value indicates the chaotic signal and a larger exponent indicates a stronger chaos [35].

Then, the time-domain responses under single-frequency sinusoidal excitation are analyzed. The time-domain response of the resonant ($f = 37.06$ Hz) and band gap ($f = 44.56$ Hz) are shown in Fig. 4(a)(c). Although the phase diagram of the waveform at 37.06 Hz seems like a quasi-periodic signal (Fig. 4(b)), its Lyapunov exponent 0.838 indicates that the responses is chaotic. In the band gap represented by 44.56 Hz, the phase diagram is highly irregular (Fig. 4(d)) and its large Lyapunov exponent 3.749 indicates a strong chaotic property.

As the time-domain method is time-consuming, mainly the frequency-domain approximate method is used below. Moreover, time-domain method is still used to confirm the responses of the optimized result. The frequency range of interest in this paper is 1–450 Hz. To evaluate the vibration reduction effect, the average value of the nonlinear vibration transmission H_{av} is selected as the objective function, which is defined as

$$H_{av} = \sum_{f=f_a}^{f_b} \Delta f \cdot H(f) / (f_b - f_a) \quad (13)$$

where f_a is the starting frequency; f_b is the stopping frequency; and Δf denotes the frequency resolution.

Meanwhile, the maximum peak value of the nonlinear vibration transmission H_p is also chosen as the reference objective function, which is defined as

$$H_p = \max(H(f)), f_a \leq f \leq f_b \quad (14)$$

Different from optimization method such as the genetic algorithm, this paper focuses on the analysis of the mechanism and regulation law of parameter. We first study the influences of different parameters on the vibration properties, and then choose the optimized parameters based on these regulars. When analyzing the influence rule of a parameter, other parameters are set according to the former analysis.

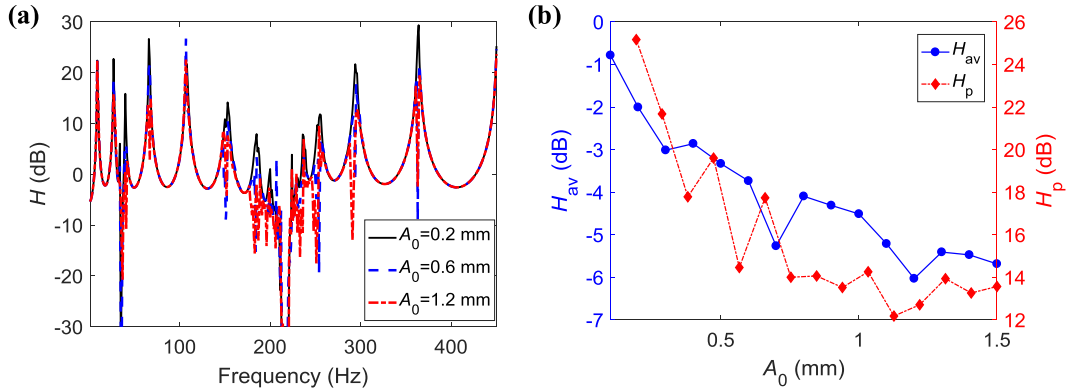


Fig. 5. The simulation results of excitation amplitude A_0 . (a) The vibration transmission curves for different A_0 ; (b) the average transmission H_{av} and the peak transmission H_p for different A_0 .

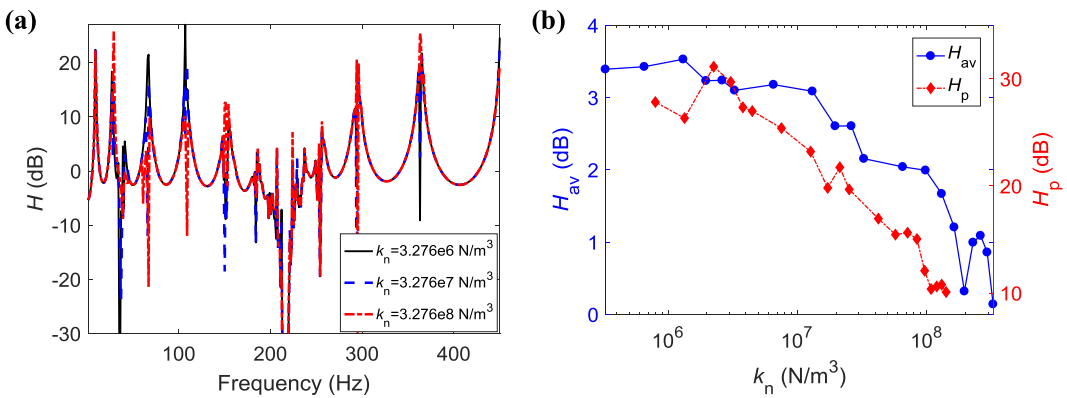


Fig. 6. The simulation results of nonlinear stiffness coefficient k_n . (a) The vibration transmission curves for different k_n ; (b) the average transmission H_{av} and the peak transmission H_p for different k_n .

4. Influences of different parameters on the vibration properties

In this paper, we systematically study the influences of the amplitude, nonlinear stiffness coefficients, resonance frequencies, attached mass and beam thickness on the bandwidth and efficiency of the vibration reduction.

4.1. Excitation amplitude A_0

The properties of NAMs depend on the driving amplitude A_0 [36]. The transmission spectra for different A_0 are shown in Fig. 5(a). Other parameter values are listed in Table 1. The linear resonances become nonlinear resonances [37] whose peak amplitudes are greatly reduced. As stronger nonlinearity is induced by larger A_0 , although the nonlinear resonances are not shifted by A_0 , the response peaks decrease with increasing A_0 . Here, H_{av} and H_p are presented by the left and right y-axes in the same figure, as shown in Fig. 5(b). Similar presentations are shown in figures below. When increasing A_0 from 0.1 to 1.5 mm, the average transmission H_{av} and the peak transmission H_p decrease by 5.3 dB and 14 dB, respectively. As confirmed in Fig. 4, these large reductions are induced by the chaotic band effect [23].

To show the influences of other factors, a moderate driving amplitude $A_0=0.6$ mm is applied in the following analyses.

4.2. Nonlinear stiffness coefficients k_n and k_c

The nonlinear stiffness coefficient also determines the nonlinear strength and then the properties of NAMs. The transmission spectra for different values of k_n are shown in Fig. 6(a). The nonlinear resonances near the first band gap LR1 decrease significantly. As shown in Fig. 6(b), when increasing k_n , both the average transmission H_{av} and the peak transmission H_p decrease monotonically. Therefore, a greater vibration reduction can be obtained by choosing the largest possible nonlinear coefficient k_n .

Then, we analyze the influence of the nonlinear coefficient k_c in torsional motion. The transmission spectra for different values of k_c are shown in Fig. 7(a). It can be seen that k_c mainly affects the vibration resonances near the second band

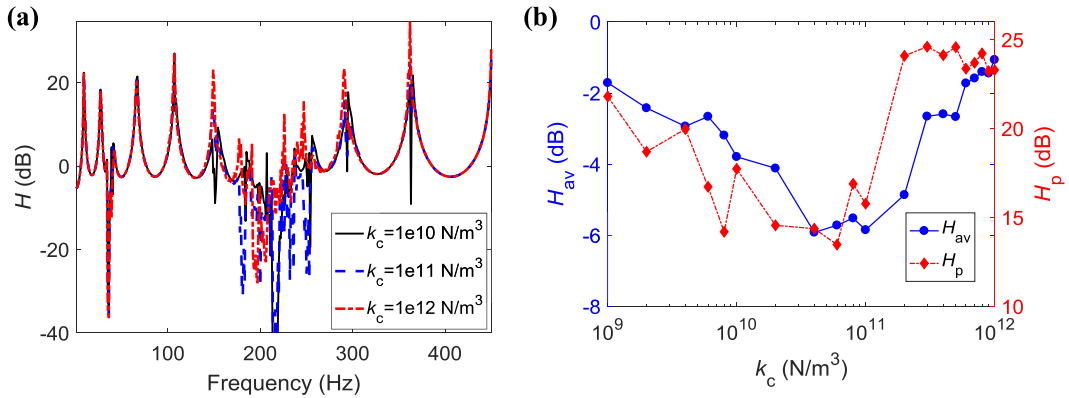


Fig. 7. The simulation results of nonlinear stiffness coefficient k_c . (a) The vibration transmission curves for different k_c ; (b) the average transmission H_{av} and the peak transmission H_p for different k_c .

gap LR2. As shown in Fig. 7(b), when increasing k_c from $1e9$ to $1e12 \text{ N m}^{-3}$, the average transmission H_{av} and the peak transmission H_p decrease first and then increase, which means that the optimal torsional nonlinear coefficient k_c depends on the excitation amplitude. When $k_c=4 \times 10^{10} \sim 10 \times 10^{10} \text{ N m}^{-3}$, the average transmission H_{av} and the peak transmission H_p are the lowest, so the optimized value can be selected within this range. The optimized value $k_c=1 \times 10^{11} \text{ N m}^{-3}$ is chosen in the following design.

4.3. Locally resonant frequencies f_{r1} and f_{r2}

As demonstrated in Ref. [30], the frequency distance between two nonlinear resonant bandgaps greatly influences the chaotic band effect, which is referred to as bridging-coupling. We shift f_{r1} and f_{r2} to clarify the bridging-coupling effect in this NAM beam.

First, f_{r1} is changed by changing the linear coefficient k_1 . The transmission spectra for different f_{r1} are shown in Fig. 8(a). The position of the first locally resonant band gap LR1 changes with f_{r1} . As shown in Fig. 8(b), when increasing f_{r1} , H_{av} decreases monotonically by approximately 3 dB, but H_p fluctuates drastically. Therefore, the vibration reduction effect exhibits little improvement. However, if the nonlinear coefficient k_2 is increased, the nonlinear effect near the first band gap LR1 will be stronger, and the effect of f_{r1} will be more significant.

Then, we analyze the influence of locally resonant frequency f_{r2} by changing the linear coefficient k_t . The second locally resonant band gap LR2 moves with f_{r2} . As shown in Fig. 8(c), the chaotic band bandwidth is significantly broadened by increasing f_{r2} . Moreover, H_{av} and H_p decrease by 11.5 dB and 18.6 dB, respectively, just by increasing f_{r2} from 200 to 400 Hz (see Fig. 8(d)). The large reductions arise from the broadened chaotic band.

4.4. Oscillator mass m_r

The attached mass is of great concern in engineering. To explore ways to reduce the attached mass of the NAM beam, we clarify the influences of the oscillator mass. Here, the frequency f_{r1} remains constant when changing the oscillator mass m_r ; i.e., k_1 is also changed. The transmission spectra for different m_r are shown in Fig. 9(a). The change in m_r mainly affects the bandwidth of LR1 and the resonant peaks in the passband. However, H_{av} decreases by only approximately 0.8 dB when increasing m_r from 5 g to 30 g (see Fig. 9(b)), which means that m_r has little impact on the vibration characteristics. This result is of paramount importance, because we can use a small attached mass to realize great vibration reduction in this case. Moreover, to reduce the attached mass of the whole system, the optimized value $m_r=5 \text{ g}$ is selected in the following optimized design.

4.5. Thickness of the NAM beam h

The thickness h represents the stiffness of the primary beam. The beam stiffness influences the bandwidth and position of the Bragg bandgap, and it also influences the coupling between the beam and nonlinear resonators. The transmission spectra for different values of h are shown in Fig. 10(a). For a thin beam (the case of $h = 2 \text{ mm}$), the Bragg bandgap is shifted from 860 Hz to 350 Hz; LR2 is also much broader than those in the aforementioned cases. In this case, H_{av} and H_p in 1~450 Hz are very small (approximately -22 dB) due to the deeper and broader bandgap. As shown in Fig. 10(b), both H_{av} and H_p increase harshly when increasing h from 2 to 2.5 mm. However, for $h>2.5 \text{ mm}$, although H_{av} still slowly increases with h , H_p exhibits fluctuations. Therefore, we have to weigh the advantages and disadvantages when increasing the beam stiffness.

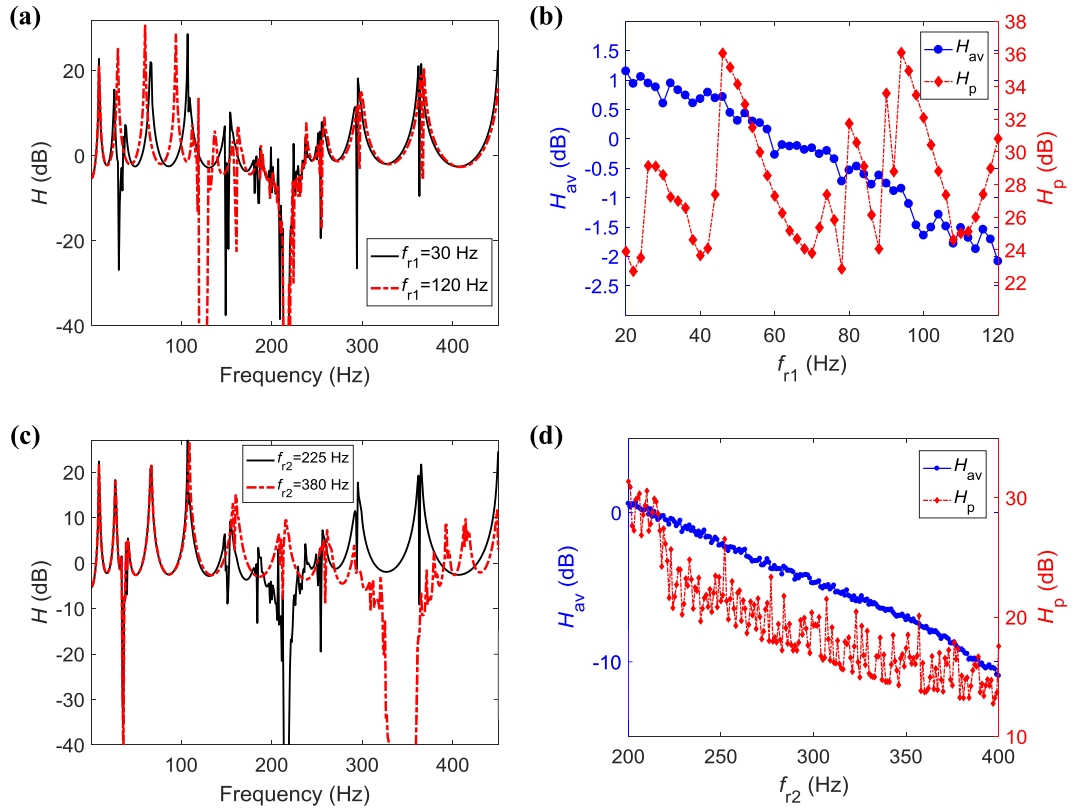


Fig. 8. The simulation results of locally resonant frequencies. (a) The vibration transmission curves for different f_{r1} ; (b) the average transmission H_{av} and the peak transmission H_p for different f_{r1} ; (c) the vibration transmission curves for different f_{r2} ; (d) the average transmission H_{av} and the peak transmission H_p for different f_{r2} .

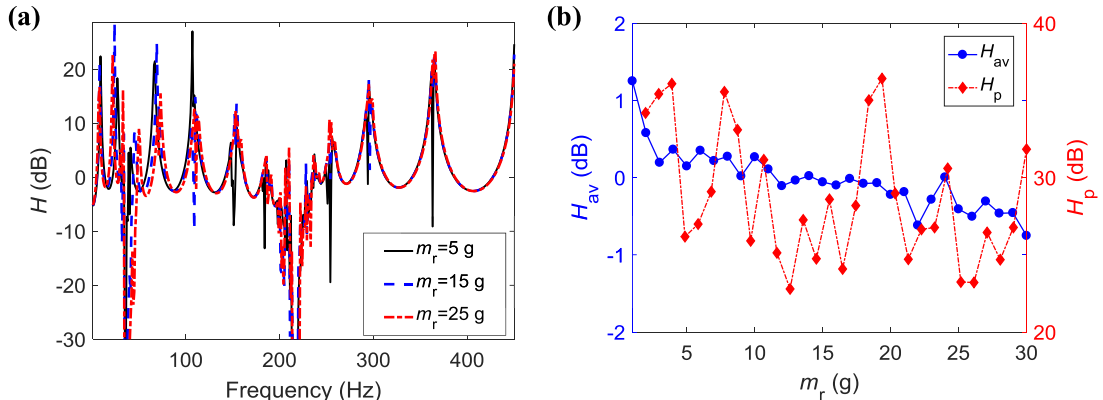


Fig. 9. The simulation results of oscillator mass m_r . (a) The vibration transmission curves for different m_r ; (b) the average transmission H_{av} and the peak transmission H_p for different m_r .

4.6. Comparing by synthesis

To compare the vibration reduction characteristics of various parameters of the NAM beam, the reductions of the average transmission H_{av} for different parameters are shown in Fig. 11. The varying ranges of the different parameters are labeled in the rectangles. It is found that the vibration transmission of the NAM beam is insensitive to the attached mass, which is helpful in reducing the weight of the structure. In addition, the vibration transmission is sensitive to the excitation amplitude, locally resonant frequency f_{r2} and nonlinear stiffness coefficients, especially f_{r2} . Therefore, by optimizing these parameters, the vibration reduction performance can be manipulated.

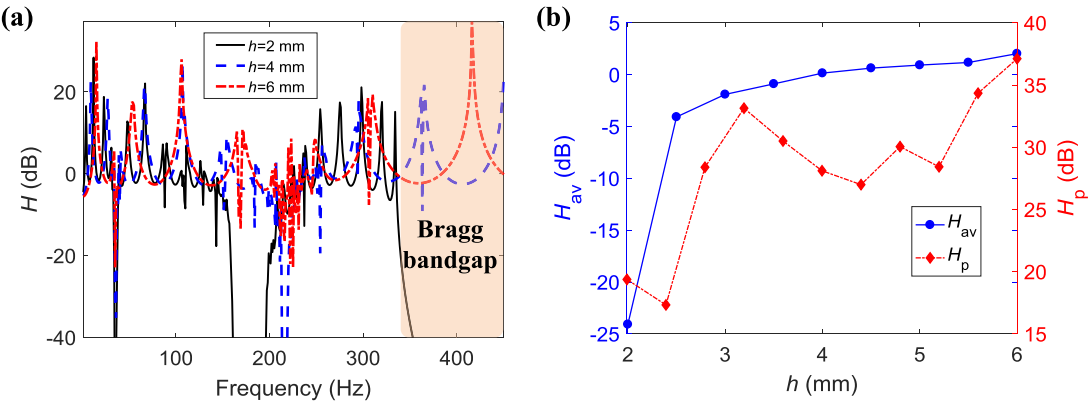


Fig. 10. The simulation results of beam thickness h . (a) The vibration transmission curves for different h ; (b) the average transmission H_{av} and the peak transmission H_p for different h .

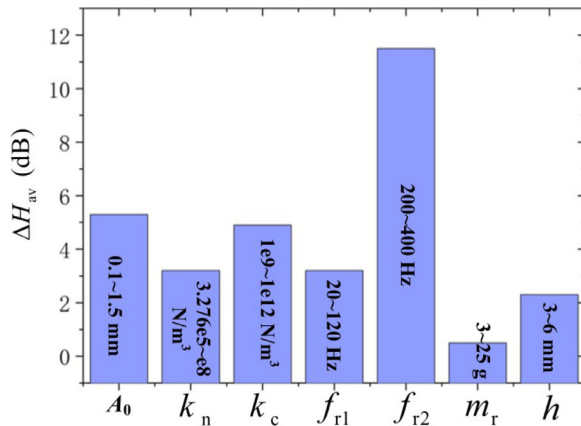


Fig. 11. Comparison of the reductions of the average transmission H_{av} for different parameters.

Table 2

The mass ratio of the initial model and optimized model.

Different model	Initial NAM beam	Optimized NAM beam
Mass ratio (%)	56.2%	28.1%

5. Optimized design

According to the above analyses, we optimize the NAM beam by choosing proper parameter values and realize it in experiment. The initial parameters are $m_r=10\text{ g}$, $f_{r2}=225\text{ Hz}$, $k_2=3.276e6\text{ N m}^{-3}$, and $k_c=1e10\text{ N m}^{-3}$. Considering the experimental realization, the optimized parameters are $m_r=5\text{ g}$, $f_{r2}=320\text{ Hz}$, $k_2=3.276e8\text{ N m}^{-3}$, and $k_c=1e11\text{ N m}^{-3}$. The other parameters are listed in Table 1. Table 2 shows the mass ratio between the attached mass of the locally resonant unit cell and the primary beam. Compared with the initial parameters, the mass ratio of the optimized parameters is reduced by half. As present in Refs [7,38], many linear acoustic metamaterials use more than 100% attached mass ratio to realize broadband reduction. This paper reduces the attached mass from 56.2% to 28.1%, which is meaningful in practice. Furthermore, because the chaotic band effect is insensitive to the attached mass, it is possible to reach a larger reduction with more elaborate resonators.

The vibration transmission spectra of the optimized result are shown in Fig. 12(a). Both the time-domain and frequency-domain solutions are provided, which are consistent except for two peaks at 58 Hz and 94 Hz. Comparing the responses of the linear and nonlinear metamaterial beam, it is obvious that nonlinearity significantly reduced the resonant peak at 30~450 Hz by 15 dB.

Moreover, great differences in the transmissions between the initial and optimized design are illustrated in Fig. 12(b). With the optimized parameters, the vibration transmission in the concerned frequency range is significantly reduced, attributing to the enhanced the chaotic band effect in optimized design. Therefore, the optimized NAM beam achieves low-frequency, broadband, and highly efficient vibration reduction with a lightweight attachment.

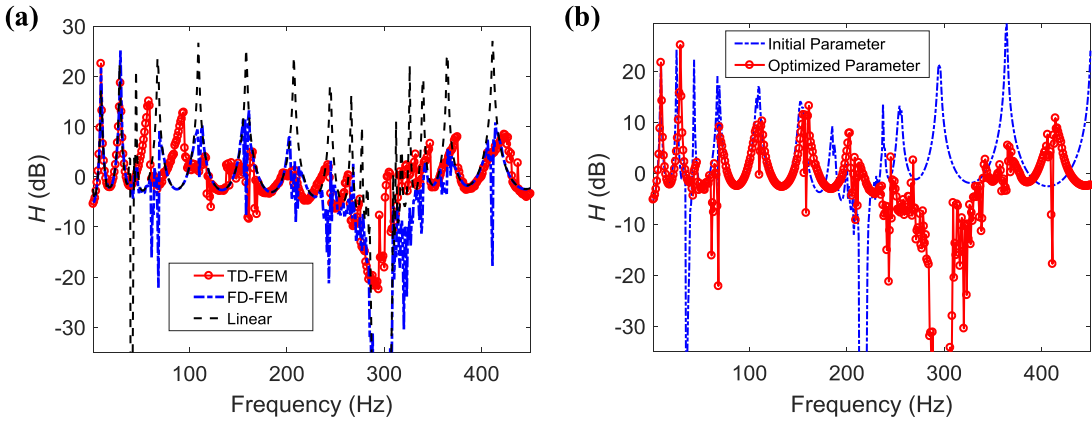


Fig. 12. The vibration property of the optimized result. (a) Comparison of the vibration transmissions obtained by the time-domain and frequency-domain finite element simulations; (b) the vibration transmissions of frequency-domain simulation with the initial parameters and optimized parameters. Here, $A_0=0.6$ mm.

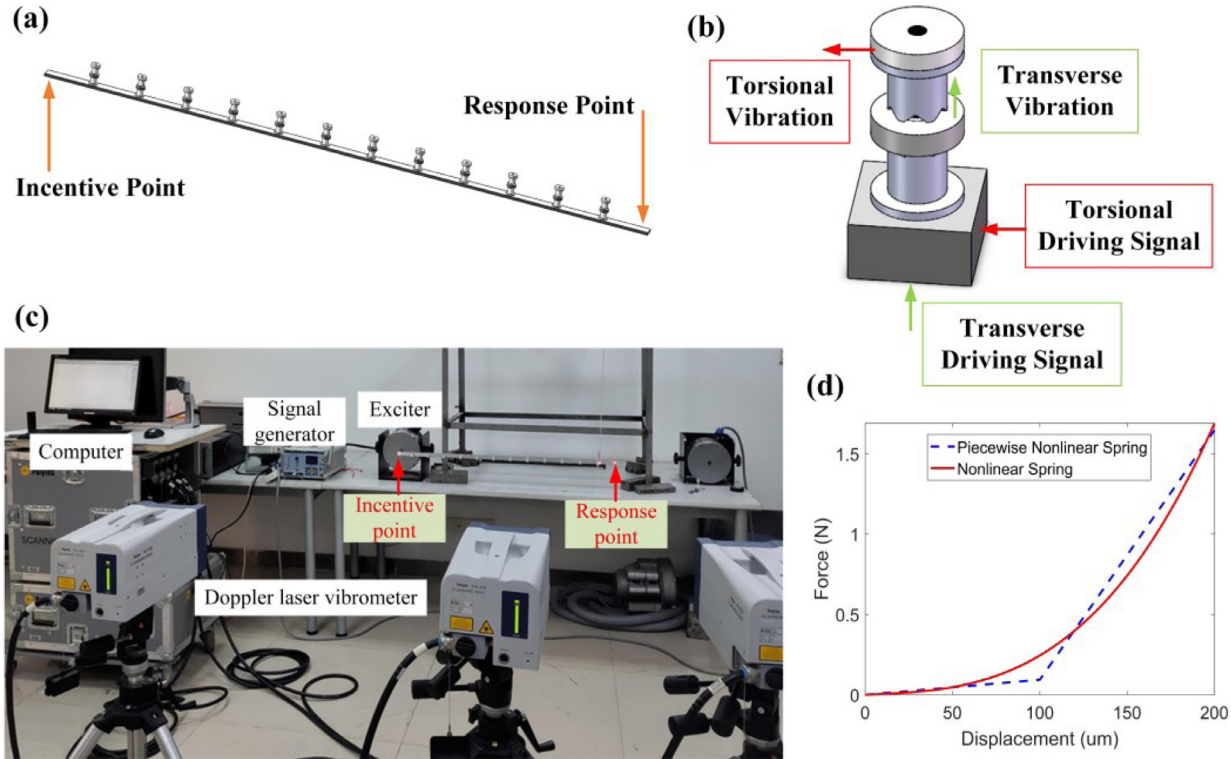


Fig. 13. Experimental model and test system. (a) NAM beam model; (b) the measuring method of transverse vibration and torsional vibration; (c) experimental test system; (d) force-displacement curve of the nonlinear spring.

6. Experimental validation

As shown in Fig. 1, this paper innovatively designs a nonlinear locally resonant unit cell, and different NAM samples are fabricated to demonstrate the optimized structure. However, the challenge lies in realizing the desired high nonlinear coefficients, k_2 and k_c , in practice. We fabricate a NAM beam consisting of 12 locally resonant unit cells, as shown in Fig. 13(a). The parameters are as follows: the thickness is $h = 4$ mm, the width is $b = 20$ mm, the lattice constant is $a = 80$ mm, and the length is $l = 040$ mm. The mass of single steel oscillator is $m_r = 4.844$ g. The stiffness of the steel spring is $k_1 = 937$ N m $^{-1}$, and $f_{r1} = 65.3$ Hz. Thickness of the thin-wall cylinder is 0.8 mm.

The clearance δ_1 between the sawtooth cylinder and the oscillator m_r is adjusted by controlling the height of the sawtooth cylinder. As shown in Fig. 13(d), the cubic nonlinear force-displacement relation can fit the real piecewise-nonlinear

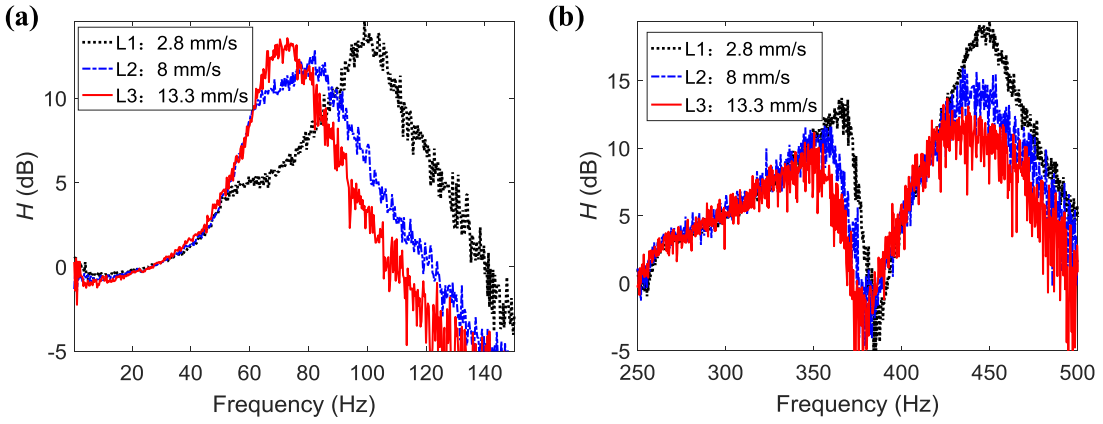


Fig. 14. Natural frequency test results. (a) Transverse motion vibration transmission; (b) torsional motion vibration transmission.

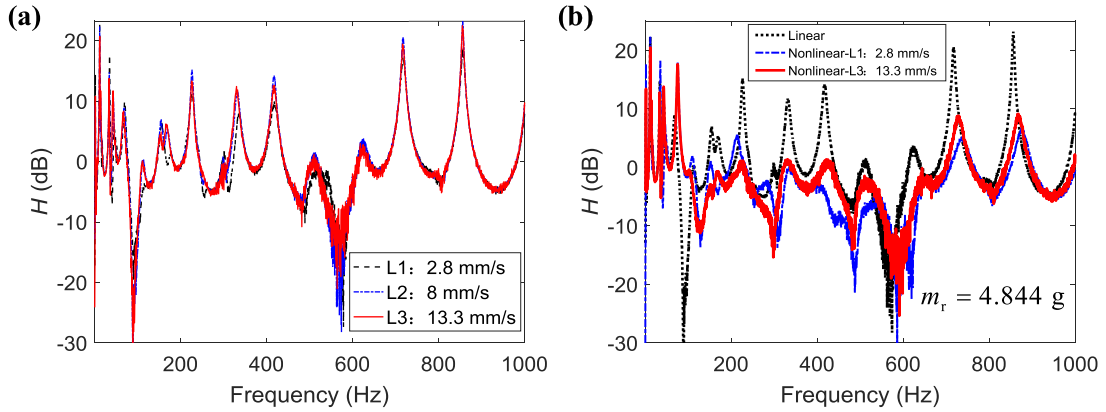


Fig. 15. Experimental results of a single oscillator. (a) Vibration transmission curves of the linear beam; (b) comparison of the linear and nonlinear vibration transmission curves.

curve well, which confirms the approximate method adopted in Section 2. A clearance δ_2 between the cylindrical support and the oscillator m_r is designed to be 0.15 mm.

The experimental system consists of a laser vibrometer, an actuator and a signal generator (Fig. 13(c)). The driving signal is white noise. The driving level (i.e., the input amplitude), is controlled by the voltage of the amplifier. The excitation spectra under different voltage are shown in Appendix C. The input amplitudes of amplifier are 2.8 mm s^{-1} , 8 mm s^{-1} and 13.3 mm s^{-1} for levels L1, L2 and L3, respectively.

First, the transverse vibration and torsional vibration of the locally resonant unit cell are measured by the laser vibrometer. The measuring method is shown in Fig. 13(b). The transmissions of the transverse and torsional vibrations are shown in Fig. 14. Increasing the driving level can shift the natural frequency of the transverse vibration from 100 Hz to 70 Hz, and can slightly reduce resonant frequencies and transmissions of torsional vibration (from 370 to 350 Hz).

For the beam, the excitation is applied at the left end of the NAM beam. The other positions of the beam are free. The vibration amplitudes of the left end and right end of the NAM beam are measured by the laser vibrometer to derive the transmission.

Firstly, we obtain a linearized metamaterial as reference by enlarging the clearance δ_1 to 1 mm and enlarging δ_2 to 0.5 mm (slightly increasing the radius of the oscillator's inner hole). The clearance δ_1 far exceeds the maximum vibration amplitude of the oscillator, so that $k_n=0$. The clearance δ_2 is also large that leads to $k_c\rightarrow 0$. This measurement makes nonlinearity negligible, i.e., a linear beam. The transmissions of this linear beam under different driving levels are shown in Fig. 15(a). The transmission spectra nearly remain constant when improving the driving amplitude.

Then, we set $\delta_1=0.1 \text{ mm}$ and $\delta_2=0.15 \text{ mm}$ to produce the two sources of clearance nonlinearity. The vibration transmissions of the nonlinear beam under different driving levels are shown in Fig. 15(b). By increasing the driving levels, the vibration reduction effect between the two locally resonant band gaps becomes more obvious. The NAM beam has a strongly nonlinear effect in the range of 90–500 Hz, so it can obviously suppress the resonances.

Furthermore, we double the oscillator mass m_r and conduct the same experiments above. As shown in Fig. 16, the low-frequency vibration reduction becomes greater for higher driving level. The NAM beam presents a strongly nonlinear effect in 70–600 Hz to suppress the resonances.

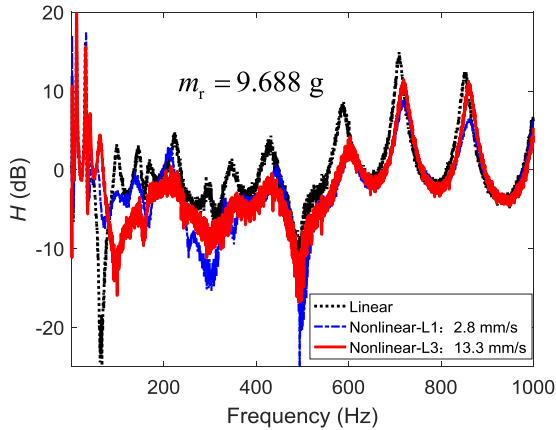


Fig. 16. Comparison of the linear and nonlinear vibration transmission curves of the two oscillators.

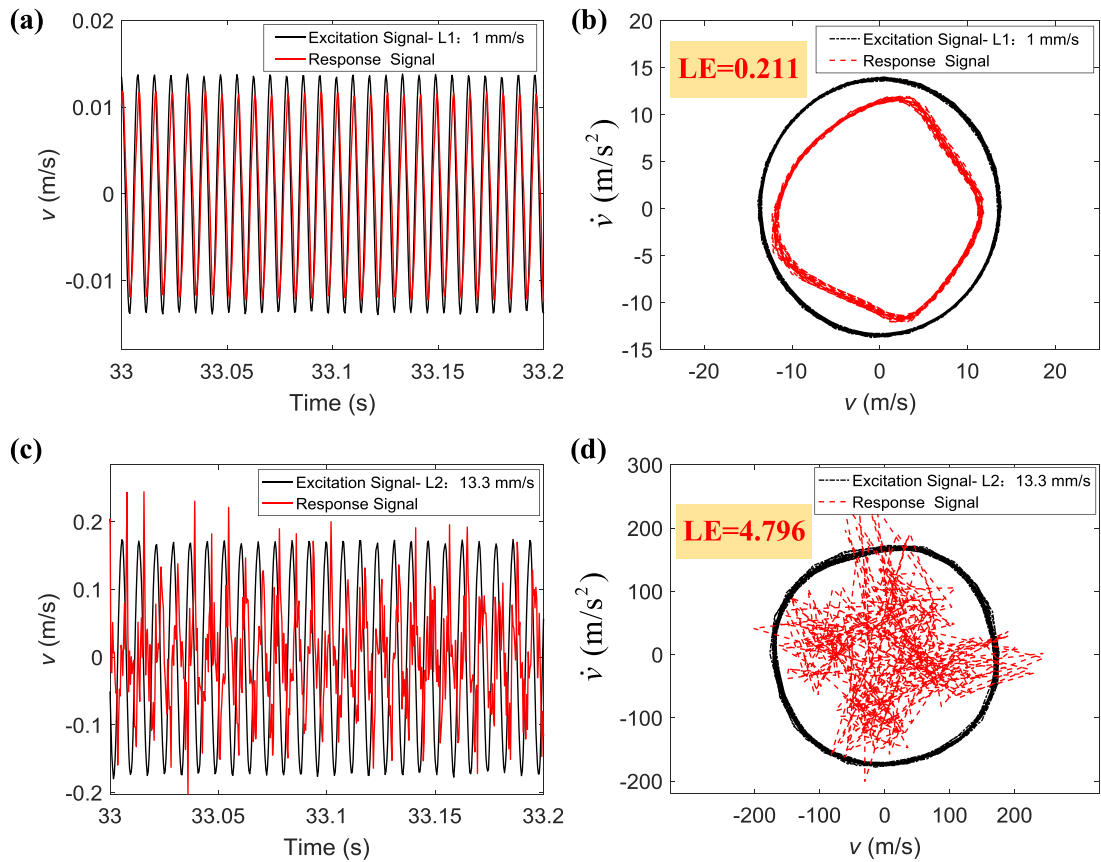


Fig. 17. Time-domain responses under a single-frequency sinusoidal excitation ($f = 127.5$ Hz). (a) Time-domain signal: driving amplitude L1 (1 mm s^{-1}); (b) the phase diagrams and maximal Lyapunov exponent: driving amplitude L1; (c) time-domain signal: driving amplitude L2 (13.3 mm s^{-1}); (d) the phase diagrams and maximal Lyapunov exponent: driving amplitude L2.

To confirm the chaotic property in experiment, we analyze the characters of the time-domain response signals under small (1 mm s^{-1}) and large (13.3 mm s^{-1}) driving amplitudes. The experiment is conducted on the nonlinear metamaterial beam with $m_r=4.844 \text{ g}$. A resonant frequency 127.5 Hz near the first bandgap is chosen for example. In this case, the standard sinusoidal signal is applied at the left end of the NAM beam, and the time-domain waveform of velocity at the right end is measured. As shown in Fig. 17(a)(b), the phase diagram and the response under the small driving amplitude L1 approximates to a quasi-periodic signal. In contrast, the highly irregular phase diagram and the large Lyapunov exponent 4.796 in Fig. 17(c)(d) indicate that the response under large driving amplitude L2 is strongly chaotic.

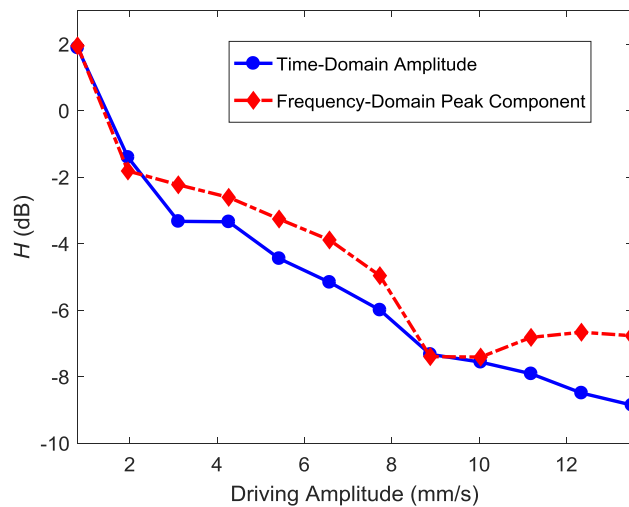


Fig. 18. The varying trends of the transmission for different driving amplitudes of amplifier (sinusoidal excitation of $f = 127.5$ Hz).

Finally, we measure the varying trends of the transmission this resonance when increasing the driving amplitude. As shown in Fig. 18, the transmissions obtained from the time-domain amplitude and frequency-domain peak component are consistent. As the driving amplitude increases, the nonlinear effect becomes stronger, and the transmission decreases. This trend also agrees with the theoretical analysis in Section 4.1.

7. Conclusions

This paper studies a finite NAM beam model including a bridging-coupling locally resonant unit cell. Both time-domain and frequency-domain finite element models are established to calculate the vibration characteristics. We systematically analyze the influences of various parameters on the bandwidth and efficiency of vibration reduction. It is found that the vibration transmission of the NAM beam is insensitive to the attached mass, which is helpful for reducing the weight of resonators. Moreover, increasing the second locally resonant frequency, excitation amplitude and nonlinear stiffness coefficients can enhance the nonlinear effects and significantly broaden the chaotic band bandwidth. According to the parameter manipulation trends, we optimize the NAM beam to realize the low-frequency, broadband, and highly efficient vibration reduction with only 28.1% attached mass. The lightweight attached mass is much smaller than the original NAM beam. Finally, we fabricate a strongly nonlinear metamaterial beam based on the optimized parameters. Both frequency-domain and time-domain experiments validate the optimized NAM structure and chaotic properties.

This work highlights important varying trends of the vibration transmission of the NAM structure when changing 6 representative parameters. These results are useful to conceive new NAM structures. The optimized design shows the great potential of NAMs for the realization of low-frequency and broadband vibration reduction with only small attachments, which is preferable in broad applications.

Declaration of Competing Interest

None.

Acknowledgments

This research was funded by the National Natural Science Foundation of China (Project nos. 12002371, 11991032 and 11991034).

Appendix A. Finite element method

For the NAM beam model described in Section 2, the FD-FEM and TD-FEM are used for the simulation to analyze the low-frequency vibration characteristics.

A1. Frequency-domain finite element method

For the transformed motion equation of Eq. (10), the frequency-domain solution can be derived with the harmonic balance method, which has been widely used in nonlinear dynamics such as the research in [31]. After obtaining the displacement response of the beam, the vibration transmission H defined by Eq. (5) is obtained. The values of the NAM beam

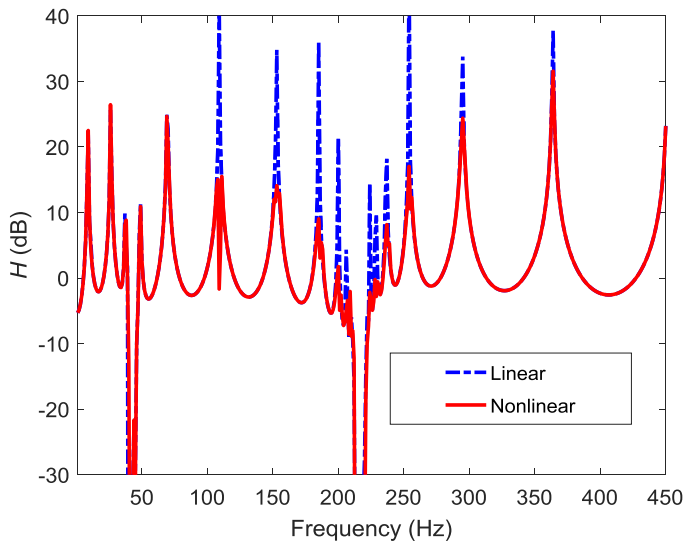


Fig. 19. Frequency-domain finite element simulation results: vibration transmissions of the linear and nonlinear model.

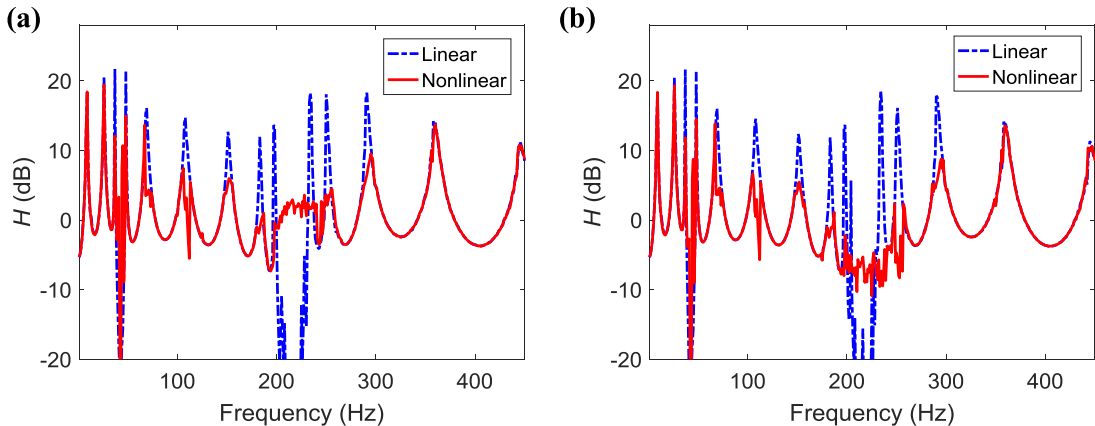


Fig. 20. Time-domain finite element simulation results. (a) The vibration transmissions obtained by the average value of the time-domain signal peak; (b) the vibration transmissions obtained by the spectrum peak.

parameters are shown in [Table 1](#), and we solve the vibration transmission curves for the linear and nonlinear finite element models in MATLAB, as shown in [Fig. 19](#).

A2. Time-domain finite element method

The NAM beam model is established in COMSOL software for the time-domain simulation. In the modeling, the physics field selects the 1D beam, point ODEs and DAE (pode) modules, and the point load is applied on the primary beam according to the system motion differential equations. The differential equations are used to simulate the locally resonant unit cell with 3 degrees of freedom. The prescribed displacement is added to the left end of the NAM beam as the excitation signal.

A single-frequency sinusoidal excitation signal is applied to the model, and we analyze the vibration characteristics after the response is stable. The simulation time is 10 s, and the sampling frequency is 1000 Hz. After the time-domain response signal is obtained by the simulation, the spectrum is analyzed, and the average value of the time-domain signal peak and spectrum peak is taken as the vibration response H in this frequency. By changing the frequency of the sinusoidal excitation signal and sweeping frequency at 1–450 Hz, the vibration transmission curve of the frequency range is obtained.

The 1–450 Hz vibration transmission curves are shown in [Fig. 20](#). The vibration transmissions obtained by time-domain signal peak and spectrum peak are similar, and the resonance frequencies and locally resonant band gap frequencies agree well with the theoretical results. However, in the second band gap, the vibration transmissions obtained by spectrum peak are smaller than those obtained by time-domain signal peak. The possible reason is that there are more harmonic components in the spectrum signal. Between and near the two band gaps, the nonlinearity has a significant effect on the reso-

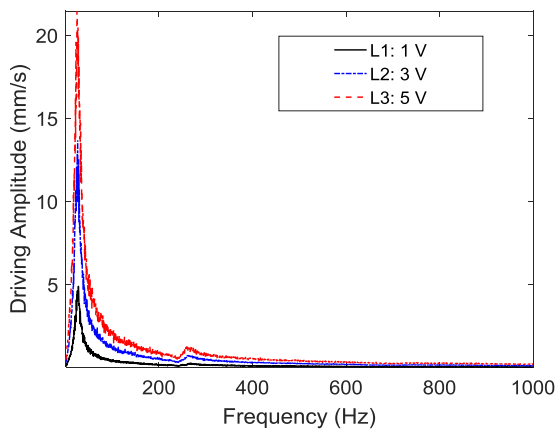


Fig. 21. The excitation spectra under different driving level, where the driving level L1: the driving voltage of amplifier is 1 V; the driving level L2: the driving voltage of amplifier is 3 V; the driving level L3: the driving voltage of amplifier is 5 V.

nances, so this method can better describe the model in this paper. The time-domain simulation in the band gap position of the linear model is unstable at some frequencies, but this does not affect the analysis of the vibration characteristics.

Appendix B. Finite element matrix

B1. Beam element

\mathbf{M}_s , \mathbf{C}_s and \mathbf{K}_s denote the mass matrix, damping matrix and stiffness matrix of beam element, respectively. Without considering the geometric nonlinearity and inertial nonlinearity of the primary beam, the finite element matrices for the flexural vibration of the beam are

$$\mathbf{M}_s = \frac{\rho l h b}{420} \begin{bmatrix} 156 & 22l & 54 & -13l \\ 22l & 4l^2 & 13l & -3l^2 \\ 54 & 13l & 156 & -22l^2 \\ -13l & -3l^2 & -22l & 4l^2 \end{bmatrix} \quad \mathbf{K}_s = \frac{EI}{l^3} \begin{bmatrix} 12 & 6l & -12 & 6l \\ 6l & 4l^2 & -6l & 2l^2 \\ -12 & -6l & 12 & -6l \\ 6l & 2l^2 & -6l & 4l^2 \end{bmatrix} \quad \mathbf{C}_s = c_0 \mathbf{K}_s$$

where $c_0=0.001/(2\pi f)$, $l = a/2$, $I=bh^3/12$, and f denotes the driving frequency.

B2. Locally resonant unit cell

\mathbf{M}_e , \mathbf{C}_e , \mathbf{K}_e and \mathbf{N}_e denote the mass matrix, damping matrix, stiffness matrix and nonlinear stiffness matrix of the locally resonant unit cell, respectively. The finite element matrices of the locally resonant unit cell are

$$\mathbf{M}_e = \begin{bmatrix} m_r & 0 & 0 & m_r & 0 \\ 0 & J_r & 0 & 0 & 0 \\ 0 & m_r l_r & m_r & 0 & 0 \\ 0 & 0 & 0 & m_0 & 0 \\ 0 & 0 & 0 & 0 & J_0 \end{bmatrix} \quad \mathbf{K}_e = \begin{bmatrix} k_1 & 0 & 0 & 0 & 0 \\ 0 & k_t & -k_3 l_r & 0 & -k_t \\ 0 & 0 & k_3 & 0 & 0 \\ -k_1 & 0 & 0 & 0 & 0 \\ 0 & -k_t & 0 & 0 & k_t \end{bmatrix}$$

$$\mathbf{N}_e = \begin{bmatrix} k_2 & 0 & 0 & 0 & 0 \\ 0 & 0 & -k_c l_r & 0 & 0 \\ 0 & 0 & k_c & 0 & 0 \\ -k_2 & 0 & 0 & 0 & 0 \\ 0 & 0 & 0 & 0 & 0 \end{bmatrix} \quad \mathbf{C}_e = \begin{bmatrix} c & 0 & 0 & 0 & 0 \\ 0 & 0 & 0 & 0 & 0 \\ 0 & 0 & 0 & 0 & 0 \\ -c & 0 & 0 & 0 & 0 \\ 0 & 0 & 0 & 0 & 0 \end{bmatrix}$$

Appendix C. Excitation spectrum

The excitation spectra as a reference value under different driving level are shown in Fig. 21.

References

- [1] S.A. Cummer, J. Christensen, A. Alù, Controlling sound with acoustic metamaterials, Nat. Rev. Mater. 1 (2016) 16001 <https://doi.org/>, doi:[10.1038/natrevmats.2016.1](https://doi.org/10.1038/natrevmats.2016.1).
- [2] K.Y. Bliokh, F. Nori, Transverse spin and surface waves in acoustic metamaterials, Phys. Rev. B 99 (2019) 020301 <https://doi.org/>, doi:[10.1103/PhysRevB.99.020301](https://doi.org/10.1103/PhysRevB.99.020301).

- [3] Z. Liu, X. Zhang, Y. Mao, Y. Zhu, Z. Yang, C. Chan, P. Sheng, Locally resonant sonic materials, *Science* 289 (2000) 1734–1736 <https://doi.org/>, doi:[10.1126/science.289.5485.1734](https://doi.org/10.1126/science.289.5485.1734).
- [4] G. Ma, P. Sheng, Acoustic metamaterials: from local resonances to broad horizons, *Sci. Adv.* 2 (2016) e1501595 <https://doi.org/>, doi:[10.1126/sciadv.1501595](https://doi.org/10.1126/sciadv.1501595).
- [5] G. Ma, M. Yang, S. Xiao, Z. Yang, P. Sheng, Acoustic metasurface with hybrid resonances, *Nat. Mater.* 13 (2014) 873–878 <https://doi.org/>, doi:[10.1038/NMAT3994](https://doi.org/10.1038/NMAT3994).
- [6] J. Zhao, B. Bonello, O. Boyko, Focusing of the lowest-order antisymmetric Lamb mode behind a gradient-index acoustic metalens with local resonators, *Phys. Rev. B* 93 (2016) 174306 <https://doi.org/>, doi:[10.1103/PhysRevB.93.174306](https://doi.org/10.1103/PhysRevB.93.174306).
- [7] M.J. Hussein, M.J. Leamy, M. Ruzzene, Dynamics of phononic materials and structures: historical origins, recent progress, and future outlook, *Appl. Mech. Rev.* 66 (2014) 040802 <https://doi.org/>, doi:[10.1115/1.4026911](https://doi.org/10.1115/1.4026911).
- [8] H. Zhang, Y. Xiao, J. Wen, D. Yu, X. Wen, Ultra-thin smart acoustic metasurface for low-frequency sound insulation, *Appl. Phys. Lett.* 108 (2016) 141902 <https://doi.org/>, doi:[10.1063/1.4945664](https://doi.org/10.1063/1.4945664).
- [9] Z. Lu, L. Cai, J. Wen, X. Chen, Physically realizable broadband acoustic metamaterials with anisotropic density, *Chin. Phys. Lett.* 36 (2019) 24301 <https://doi.org/>, doi:[10.1088/0256-307X/36/2/024301](https://doi.org/10.1088/0256-307X/36/2/024301).
- [10] N. Higashiyama, Y. Doi, A. Nakatani, Nonlinear dynamics of a model of acoustic metamaterials with local resonators, *Nonlinear Theory Applica.* 8 (2016) 129–145 <https://doi.org/>, doi:[10.1587/nolta.8.129](https://doi.org/10.1587/nolta.8.129).
- [11] L. Cveticanin, M. Zukovic, Negative effective mass in acoustic metamaterial with nonlinear mass-in-mass subsystems, *Commun. Nonlinear Sci. Numer. Simul.* 51 (2017) 89–104 <https://doi.org/>, doi:[10.1016/j.cnsns.2017.03.017](https://doi.org/10.1016/j.cnsns.2017.03.017).
- [12] T. Dauxois, Fermi, Pasta, Ulam, and a mysterious lady, *Phys. Today* 61 (2008) <https://doi.org/>, doi:[10.1063/1.2835154](https://doi.org/10.1063/1.2835154).
- [13] W. Zhou, X. Li, Y. Wang, W. Chen, G. Huang, Spectro-spatial analysis of wave packet propagation in nonlinear acoustic metamaterials, *J. Sound Vib.* 413 (2018) 250–269 <https://doi.org/>, doi:[10.1016/j.jsv.2017.10.023](https://doi.org/10.1016/j.jsv.2017.10.023).
- [14] A.F. Vakakis, M.A. AL-Shudeifat, M.A. Hasan, Interactions of propagating waves in a one-dimensional chain of linear oscillators with a strongly nonlinear local attachment, *Mecchanica* 49 (2014) 2375–2397 <https://doi.org/>, doi:[10.1007/s11012-014-0008-9](https://doi.org/10.1007/s11012-014-0008-9).
- [15] L. Bonanomi, G. Theocharis, C. Daraio, Wave propagation in granular chains with local resonances, *Phys. Rev. E* 91 (2015) 033208 <https://doi.org/>, doi:[10.1103/PhysRevE.91.033208](https://doi.org/10.1103/PhysRevE.91.033208).
- [16] P.B. Silva, M.J. Leamy, M. Geers, V.G. Kouznetsova, Emergent subharmonic band gaps in nonlinear locally resonant metamaterials induced by autoparametric resonance, *Phys. Rev. E* 99 (2019) 063003 <https://doi.org/>, doi:[10.1103/PhysRevE.99.063003](https://doi.org/10.1103/PhysRevE.99.063003).
- [17] M.D. Fronk, M.J. Leamy, Higher-order dispersion stability, and waveform invariance in nonlinear monoatomic and diatomic systems, *J. Vib. Acoust.* 139 (2017) 051003 <https://doi.org/>, doi:[10.1115/1.4036501](https://doi.org/10.1115/1.4036501).
- [18] K. Manktelow, R.K. Narisetti, M.J. Leamy, M. Ruzzene, Finite-element based perturbation analysis of wave propagation in nonlinear periodic structures, *Mech. Syst. Signal Process.* 39 (2013) 32–46 <https://doi.org/>, doi:[10.1016/j.ymssp.2012.04.015](https://doi.org/10.1016/j.ymssp.2012.04.015).
- [19] R. Khajehhtourian, M.I. Hussein, Damping and nonlinearity in elastic metamaterials: treatment and effects, *AIP Adv.* 4 (2014) 124308 <https://doi.org/>, doi:[10.1121/1.4877386](https://doi.org/10.1121/1.4877386).
- [20] O.R. Bilal, A. Foehr, C. Daraio, Bistable metamaterial for switching and cascading elastic vibrations, *Proc. Natl. Acad. Sci.* 114 (2017) 4603–4606 <https://doi.org/>, doi:[10.1073/pnas.1618314114](https://doi.org/10.1073/pnas.1618314114).
- [21] D. Hatanaka, T. Darras, I. Mahboob, K. Onomitsu, H. Yamaguchi, Broadband reconfigurable logic gates in phonon waveguides, *Sci. Rep.* 7 (2017) 12745 <https://doi.org/>, doi:[10.1038/s41598-017-12654-3](https://doi.org/10.1038/s41598-017-12654-3).
- [22] F. Li, P. Anzel, J. Yang, P.G. Kevrekidis, C. Daraio, Granular acoustic switches and logic elements, *Nat. Commun.* 5 (2014) 5311 <https://doi.org/>, doi:[10.1038/ncomms6311](https://doi.org/10.1038/ncomms6311).
- [23] X. Fang, J. Wen, B. Bonello, J. Yin, D. Yu, Ultra-low and ultra-broad-band nonlinear acoustic metamaterials, *Nat. Commun.* 8 (2017) 1288 <https://doi.org/>, doi:[10.1038/s41467-017-00671-9](https://doi.org/10.1038/s41467-017-00671-9).
- [24] X. Fang, J. Wen, H. Benisty, D. Yu, Ultrabroad acoustical limiting in nonlinear metamaterials due to adaptive-broadening band-gap effect, *Phys. Rev. B* 101 (2020) 104304 <https://doi.org/>, doi:[10.1103/PhysRevB.101.104304](https://doi.org/10.1103/PhysRevB.101.104304).
- [25] P.F. Pai, H. Peng, S. Jiang, Acoustic metamaterial beams based on multi-frequency vibration absorbers, *Int. J. Mech. Sci.* 79 (2014) 195–205 <https://doi.org/>, doi:[10.1016/j.ijmecsci.2013.12.013](https://doi.org/10.1016/j.ijmecsci.2013.12.013).
- [26] V. Romero-García, A. Krynkin, L.M. García-Raffi, O. Umnova, J.V. Sánchez-Pérez, Multi-resonant scatterers in sonic crystals: locally multi-resonant acoustic metamaterial, *J. Sound Vib.* 332 (2013) 184–198 <https://doi.org/>, doi:[10.1016/j.jsv.2012.08.003](https://doi.org/10.1016/j.jsv.2012.08.003).
- [27] A. Luongo, D. Zulli, Dynamic analysis of externally excited NES-controlled systems via a mixed Multiple Scale/Harmonic Balance algorithm, *Nonlinear Dyn.* 70 (2012) 2049–2061 <https://doi.org/>, doi:[10.1007/s11071-012-0597-6](https://doi.org/10.1007/s11071-012-0597-6).
- [28] T.F. van Nuland, P.B. Silva, A. Sridhar, M.G. Geers, V.G. Kouznetsova, Transient analysis of nonlinear locally resonant metamaterials via computational homogenization, *Math. Mech. Solid.* 24 (2019) 3136–3155 <https://doi.org/>, doi:[10.1177/1081286519833100](https://doi.org/10.1177/1081286519833100).
- [29] X. Fang, J. Wen, B. Bonello, J. Yin, D. Yu, Wave propagation in one-dimensional nonlinear acoustic metamaterials, *New J. Phys.* 19 (2017) 053007 <https://doi.org/>, doi:[10.1088/1367-2630/aa6d49](https://doi.org/10.1088/1367-2630/aa6d49).
- [30] X. Fang, J. Wen, D. Yu, J. Yin, Bridging-Coupling band gaps in nonlinear acoustic metamaterials, *Phys. Rev. Appl.* 10 (2018) 054049 <https://doi.org/>, doi:[10.1103/PhysRevApplied.10.054049](https://doi.org/10.1103/PhysRevApplied.10.054049).
- [31] X. Fang, J. Wen, J. Yin, D. Yu, Y. Xiao, Broadband and tunable one-dimensional strongly nonlinear acoustic metamaterials: theoretical study, *Phys. Rev. E* 94 (2016) 052206 <https://doi.org/>, doi:[10.1103/PhysRevE.94.052206](https://doi.org/10.1103/PhysRevE.94.052206).
- [32] X. Fang, J. Wen, J. Yin, D. Yu, Wave propagation in nonlinear metamaterial multi-atomic chains based on homotopy method, *AIP Adv.* 6 (2016) 121706 <https://doi.org/>, doi:[10.1063/1.4971761](https://doi.org/10.1063/1.4971761).
- [33] B.S. Lazarov, J.S. Jensen, Low-frequency band gaps in chains with attached non-linear oscillators, *Int. J. Non Linear Mech.* 42 (2007) 1186–1193 <https://doi.org/>, doi:[10.1016/j.ijnonlinmec.2007.09.007](https://doi.org/10.1016/j.ijnonlinmec.2007.09.007).
- [34] H. Kantz, A robust method to estimate the maximal Lyapunov exponent of a time series, *Phys. Lett. A* 185 (1994) 77–87 <https://doi.org/>, doi:[10.1016/0375-9601\(94\)90991-1](https://doi.org/10.1016/0375-9601(94)90991-1).
- [35] J. Eckmann, S.O. Kamphorst, D. Ruelle, S. Ciliberto, Liapunov exponents from time series, *Phys. Rev. A* 34 (1986) 4971–4979 <https://doi.org/>, doi:[10.1103/PhysRevA.34.4971](https://doi.org/10.1103/PhysRevA.34.4971).
- [36] C. Daraio, V.F. Nesterenko, E. Herbold, S. Jin, Tunability of solitary wave properties in one-dimensional strongly nonlinear phononic crystals, *Phys. Rev. E* 73 (2006) 026610 <https://doi.org/>, doi:[10.1103/PhysRevE.73.026610](https://doi.org/10.1103/PhysRevE.73.026610).
- [37] J. Lydon, G. Theocharis, C. Daraio, Nonlinear resonances and energy transfer in finite granular chains, *Phys. Rev. E* 91 (2015) 023208 <https://doi.org/>, doi:[10.1103/PhysRevE.91.023208](https://doi.org/10.1103/PhysRevE.91.023208).
- [38] Y. Xiao, J. Wen, G. Wang, X. Wen, Theoretical and experimental study of locally resonant and Bragg band gaps in flexural beams carrying periodic arrays of beam-like resonators, *J. Vib. Acoust.* 135 (2013) 041006 <https://doi.org/>, doi:[10.1115/1.4024214](https://doi.org/10.1115/1.4024214).